Solid State Phenomena
ISSN: 1662-9779, Vol. 389, pp 191-206
doi:10.4028/p-Y78kVu

Submitted: 2026-01-19
Revised: 2026-02-22
Accepted: 2026-02-24
Online: 2026-04-16

Multi-Stage Roller Embossing of Bipolar Plate Microchannels Using 3D-Printed Tooling

Maziar Khademi[1,a*], Peng Neo Zhang[1,b], Michael P. Pereira[2,c] and Matthias Weiss[1,d]

[1]Institute for Frontier Materials, Deakin University, 75 Pigdons Rd., Waurn Ponds, Geelong, VIC 3216, Australia

[2]School of Engineering, Deakin University, 75 Pigdons Rd., Waurn Ponds, Geelong, VIC 3216, Australia

[a]m.khademi@deakin.edu.au, [b]peng.neo.zhang@deakin.edu.au, [c]michael.pereira@deakin.edu.au [d]matthias.weiss@deakin.edu.au,

Keywords: Bipolar plates; 3D Printed tool; Micro-roller embossing; Fuel cell; Multi stage forming.

Abstract. Bipolar plates are key components in fuel cells, and their performance strongly depends on the geometry of the microchannels used to distribute reactant gases. Producing channels with sufficient depth in thin metal sheets remains challenging, particularly when cost-effective manufacturing routes are required. This work investigates a multi-stage roller embossing process for forming bipolar plate channels using additively manufactured polymer tools. By dividing the total deformation into multiple forming stages, the process reduces tool deflection that typically limits channel depth in single-pass embossing. Experiments conducted on 0.1 mm stainless steel foil show that the multi-stage approach increases the achievable average channel depth from approximately 0.25 mm in a single pass to approximately 0.34 mm, resulting in a maximum aspect ratio (channel depth to width) of 0.314. These results indicate that combining multi-stage forming with 3D-printed tooling provides a practical route for flexible and low-cost fabrication of metallic bipolar plates, especially for low volume production.

Introduction

Proton Exchange Membrane Fuel Cells (PEMFCs) generate electricity from hydrogen and oxygen and only produce water as a byproduct. A typical PEMFC stack unit consists of different components, including the bipolar plates (BPPs), which have a large number of small flow channels (microchannels) for the gases to interact [1]. The performance of the fuel cell is influenced by the geometry of the microchannels within the BPPs. A key geometrical parameter is the aspect ratio (AR) of the channels, which is the ratio of channel depth to width, which directly influences the efficiency of fuel cells [2]. Despite extensive research on bipolar plate fabrication, achieving high aspect ratio microchannels in thin metallic foils remains a key manufacturing challenge. Mass production of metal BPPs is often achieved using micro-stamping, but this process can lead to issues such as wrinkling defects and material thinning or even rupture [3]. Research has shown that the maximum achievable aspect ratio for stainless steel with thickness of 0.1 mm using micro-stamping is 0.43 [4] – i.e., micro-stamping is limited by the maximum aspect ratio that can be achieved. These limitations motivate the exploration of alternative forming processes that can reduce material thinning and forming defects, while enabling greater channel depths and hence higher aspect ratios.

Micro roll forming has been shown to reduce material thinning [1] and Bauer et al. [5] has shown that the micro roller embossing process can be used to form BPPs on an industrial scale. By utilizing a rolling mill, Bauer et al. [5] formed 0.1 mm-thick stainless steel foils successfully in a single pass. However, the process showed forming defects in the form of wrinkles. The main challenge in the work by Bauer et al. [5] is that the reported formed depth of 0.31 mm is lower than the target depth of 0.5 mm. A similar limitation was observed when forming more complex channel patterns using roller embossing [6]. This issue appears to be related to structural deflection, particularly shaft deflection, occurring during the roller embossing process even when steel tools are used. This

observation indicates that tool and shaft deflection can play a dominant role in limiting the achievable channel depth.

In general, increasing the forming depth requires higher forming forces, which in turn increases the stresses that must be transferred at the channel corner radii. Rather than increasing forming forces in a single pass, distributing deformation over multiple forming steps provides a promising strategy to overcome depth and deflection limitations.

One effective way to reduce stress and thereby increase the achievable aspect ratio is to increase the number of forming steps. Multi-stage forming reduces the forming force that must be transferred in each step. It also enables the creation of intermediate shapes that promote material flow and allows higher stresses to be transferred at the channel corners [7, 8]. As a result, multi-stage forming has the potential to increase the achievable aspect ratio while reducing peak stresses on both the material and the forming tools.

In recent years, additive manufacturing has gained recognition as a viable technology for rapid prototyping of forming tools [9]. Various studies have explored the use of 3D-printed tools for sheet metal forming processes, such as V-bending of aluminum [10] and deep drawing of aluminum and steel [8]. The findings indicate that 3D-printed plastic tools are capable of forming metal sheets, but tool deflection during forming presents a major challenge [11]. This challenge is particularly critical in micro-forming applications, where the magnitude of small tool deflections (e.g. fractions of a millimeter) can be a large percentage of the total forming height; thus, leading to large deviations in the formed channel geometry. Cyron et al. [12] investigated the fabrication of BPPs using plastic dies, demonstrating that 3D-printed plastic tools can be employed for micro-component forming. However, a comparison between conventionally machined steel dies and 3D-printed plastic dies revealed notable discrepancies between the designed and actual plate shapes that were formed with plastic tools. The underlying causes of these deviations were not analysed.

To date, no work has systematically combined multi-stage roller embossing with additively manufactured tooling, while explicitly accounting for tool deflection effects. In this study, the 3D printing concept is applied to a new concept of the roller embossing process (named multi-stage roller embossing), to form a representative BBP geometry using stainless steel foil. Three forming strategies are examined: single-stage forming with ABS tooling, multi-stage forming with ABS tooling, and multi-stage forming with a stiffer photopolymer resin insert in the final stage. A Finite Element Analysis (FEA) model was developed and used to prove the concept and validated with experimental results. The FEA model was then used to develop a solution for redesigning the tool setup and geometry to reduce tool deflection effects and reduce the forming force in the roller embossing process to increase the forming depth. The results of this study suggests that 3D printed plastic forming tools can be used to form microchannels relevant to BPP production if tool deflection is accounted for.

Experiment Set Up

Material. The study utilised bright-annealed 316L stainless steel foil with a thickness of 0.1 mm. The mechanical properties of the 316L stainless steel were obtained from a previous study [13] where the true stress-strain curve was determined and fitted with the Swift law (Eq. 1):

$$\sigma=k(\varepsilon_0+\varepsilon)^n \quad (1)$$

where K, ε_0 and n, are the strength coefficient, strain shift parameter, and hardening exponent, respectively. The anisotropic plastic behaviour was characterised using the Lankford coefficients r_0, r_{45}, and r_{90}, corresponding to rolling, diagonal, and transverse directions, respectively. The elastic and plastic properties are presented in Table 1.

Table 1. Elastic and plastic property parameters of the 316 L stainless steel sheet [13].

E (GPa)	K	n	ε_0	r_0	r_{45}	r_{90}
190	1534	0.516	0.047	0.85	1.22	1.21

Acrylonitrile butadiene styrene (ABS) and a rigid photopolymer resin (Formlabs Rigid 10K resin [14]) were used for the 3D-printed tools. The ABS material was supplied by Stratasys Ltd [15]. All ABS parts in this study were additively manufactured using a Stratasys F190 fused deposition modelling 3D printer, with a 100% infill strategy and a layer thickness of 0.127 mm. The Rigid 10K resin is a glass-filled photopolymer with high stiffness and strength, designed for tooling and functional prototyping applications, and was supplied by Formlabs Inc. All Rigid 10k resin parts in this study were additively manufactured using a Formlabs 3L 3D printer, which uses low force stereolithography technology, with a layer height of 50 µm. After printing, all Rigid 10K resin specimens were post-cured using the manufacturer's recommended procedure. The post-curing process was conducted at a temperature of 70 °C for a duration of 60 minutes to ensure complete polymerization, enabling the material to reach its intended stiffness, strength, and heat resistance.

The ABS and Rigid 10k resin materials were tested in compression according to ASTM-D1621 standard [16] using cuboid samples (Fig. 1). The compressive load was applied parallel to the material stacking direction (z-axis). The specimens were printed with the build direction aligned with the z-axis, such that the layer stacking direction was parallel to the applied compressive load.

Fig. 2 shows the resulting compressive stress-strain curve. The elastic modulus determined from the stress strain response was 1.3 GPa and 5.7 GPa for ABS and Rigid 10K resin, respectively, where the reported values represent the average of five tested specimens for each material. When manufactured using 3D printing, the Poisson's ratio of the ABS material is reported to be 0.37 [17], and 0.36 for Rigid 10k resin [18].

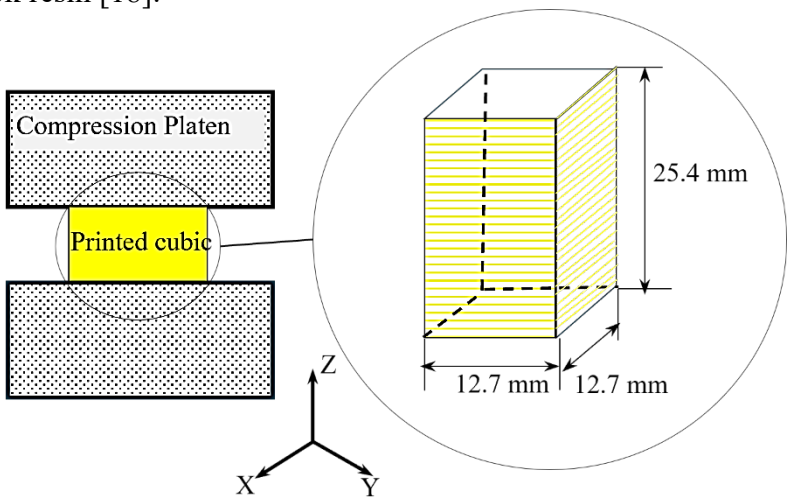

Fig. 1. Schematic of the compression tests and compression test samples used to characterise the 3D printed materials.

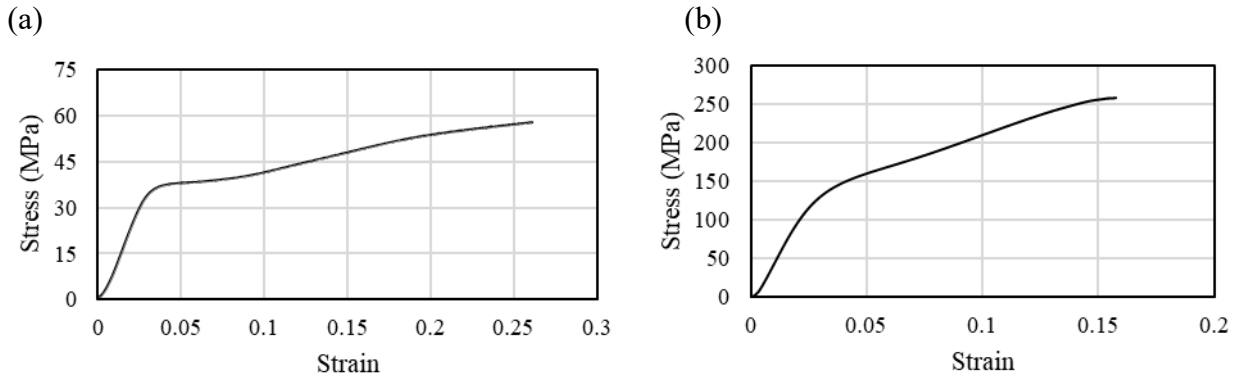

Fig. 2. Engineering stress-strain curves, determined in the compression tests, for the 3D-printed materials: a) ABS, b) Rigid 10K resin.

Experimental micro roller embossing trials. The ideal cross-section of the microchannels, formed with an aspect ratio of 0.462 calculated based on the method described in [19], is shown in

Fig. 3. This profile was selected based on previous research [5] performed on BPP forming with steel tools, enabling a comparison of the results. The dimensions of the forming rollers are shown in Fig. 4(a). The forming was conducted on a mini roll former that is chain-driven using three stations (see Fig. 4(c) and (d)). Stations 1, 2, and 3 are used sequentially in the multi-stage forming process, with each station contributing to the progressive forming of the microchannels in the sheet. In addition, the guide stations ensure stable sheet alignment and controlled material feeding between forming stages. The roller gap between the top and bottom rollers was set at 0.1 mm and a flat sheet (170 mm length × 27 mm width) was fed into the roller former.

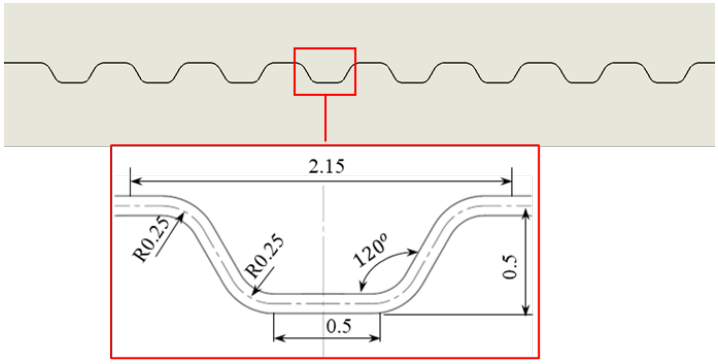

Fig. 3. Schematic of the target microchannel profile, units of the linear dimensions in millimetres.

(a)

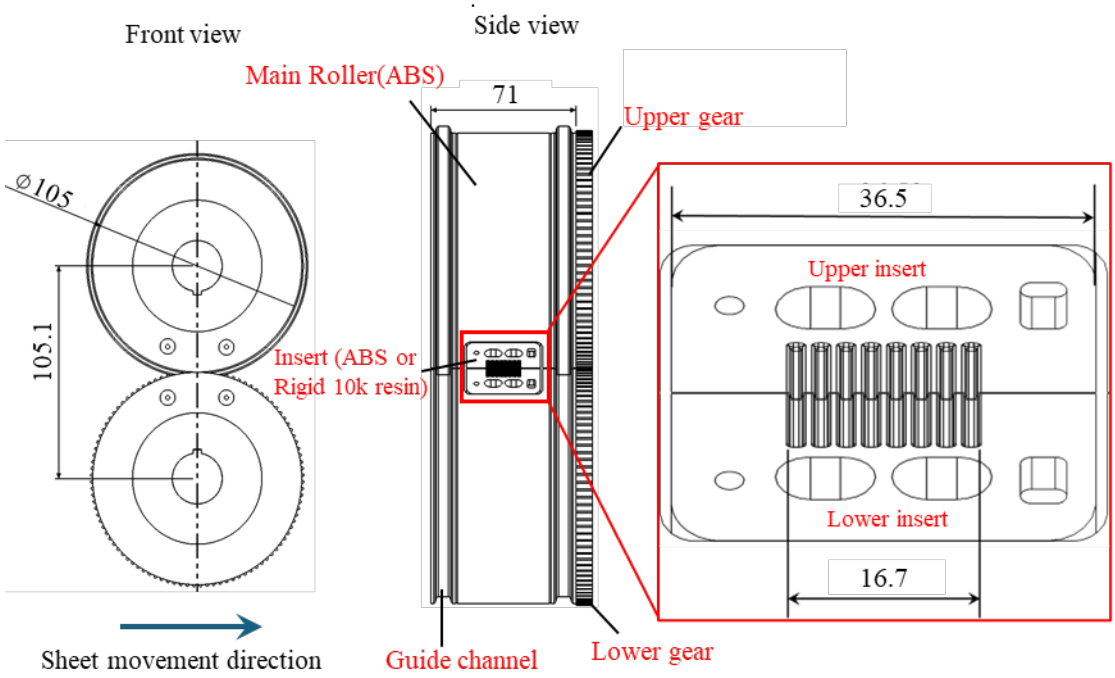

(b)

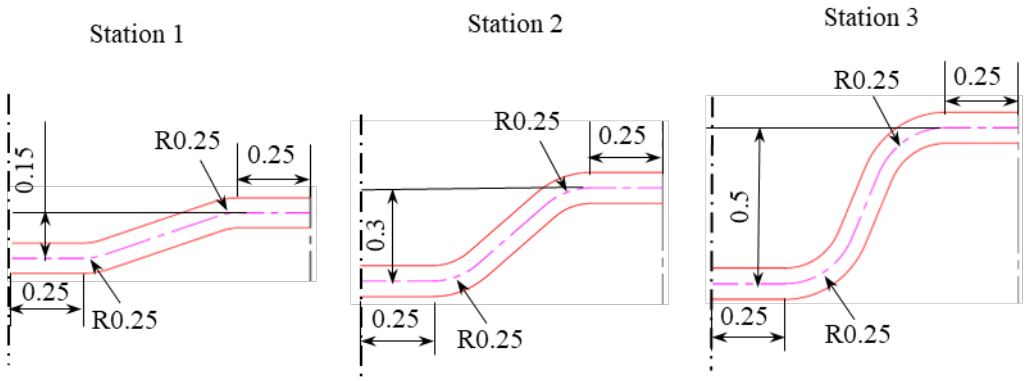

(c)

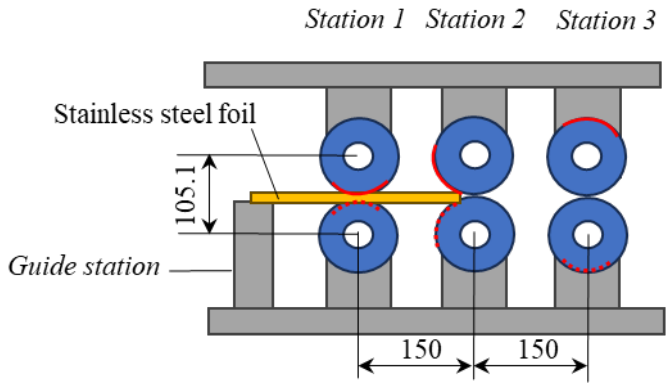

(d)

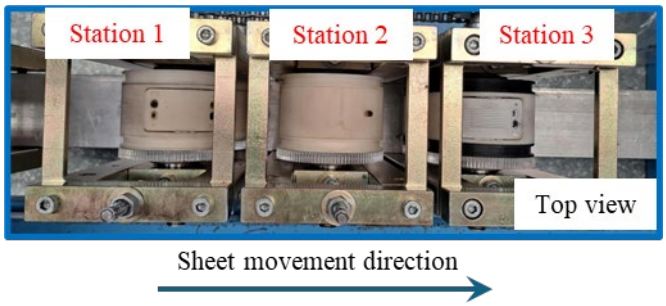

Fig. 4. a) Schematic of the micro roller embossing tooling for single roller station. b) Desired cross-section of tool in each station (dimensions in mm). c) Schematic of the three-station roller embossing layout, illustrating the relative position of the top and bottom rollers and the stainless-steel foil feed path through the guide station. d) Photograph from the top of the experimental roller former.

To evaluate the influence of multi-stage forming on channel quality, three sequential forming depths of 0.15 mm, 0.30 mm and 0.50 mm (shown in Fig. 4(b)) were first tested using ABS-based 3D-printed tooling. This series was designed to quantify the effect of incrementally increasing deformation during the forming process. Following this, an additional sequence was conducted in which the initial two steps (0.15 mm and 0.30 mm depth) were performed with ABS tooling, while the final forming step (0.50 mm depth) was conducted using a resin-based tool. This second test condition was intended to demonstrate the feasibility of forming micro-channels using hybrid 3D-printed tooling materials and to provide evidence supporting the applicability of resin tooling for the final, higher-load forming stage. The three investigated forming strategies are defined as Cases A–C and summarised in Table 2, which introduces the case labels, forming strategies, and corresponding tooling configurations used throughout the remainder of the study.

Table 2. Summary of the different forming strategies and tooling configurations used in this study, which are designed to achieve increased forming depth.

Case	Forming strategy	Tooling configuration
A	Single-stage forming	ABS inserts
B	Multi-stage forming (3 stages)	ABS inserts (all 3 stages)
C	Multi-stage forming (3 stages)	ABS inserts + Rigid 10k resin (final stage)

The final shape of the profiles and the dimensional accuracy of the 3D-printed rollers were analysed using a non-contact optical surface profilometer Alicona®, with a 5× magnification optical lens, a vertical resolution of 360 nm and a lateral resolution of 3.91 µm. The Mean Absolute Error (MAE) [20] value was determined to quantify the deviation between the actual and printed roller profiles. Following the methodology outlined in [20], the MAE determined for the top and bottom roller profiles was 37 µm and 26 µm, and 19 µm and 29 µm for Rigid 10k resin tools respectively, suggesting that the rollers were printed with high precision.

Numerical Analysis

FEA of the roller embossing forming process was conducted with ABAQUS. All parts of the experimental micro roller embossing set up were replicated in the numerical model, including the dimensions of the rollers, sheet length, and roller gap. The FEA model is shown in Fig. 5. As shown, each roller consists of two parts: the main rollers and the inserts. The main rollers are made of ABS; however, depending on the forming strategy, the material of the inserts differs. Therefore, in the numerical simulation, separate sections were defined to assign different material properties to the rollers and inserts.

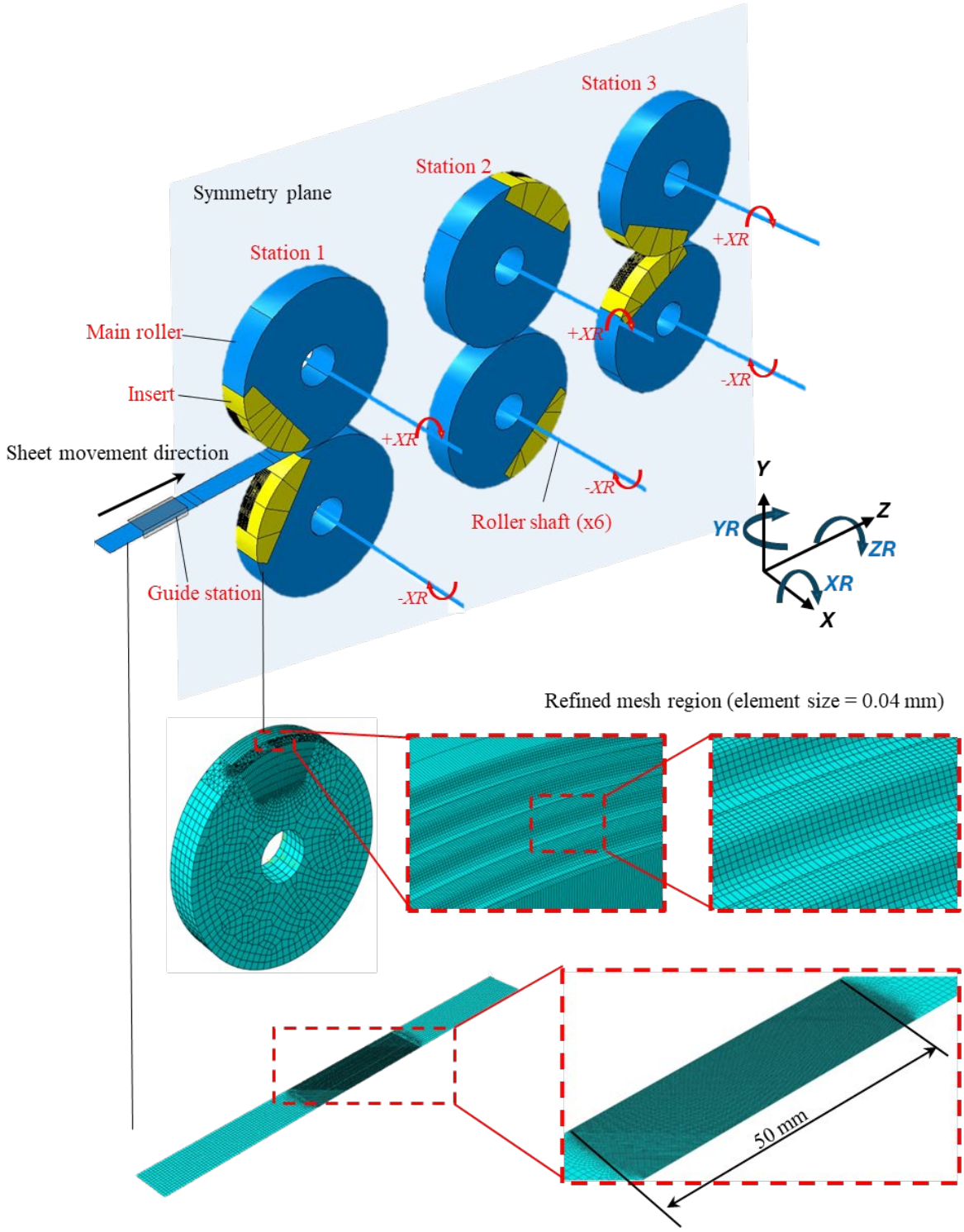

Fig. 5. FEA model of the multi-stage micro roller embossing process.

The sheet was meshed with S4R shell elements, with 5 integration points through the material thickness. Based on the mesh sensitivity analysis shown in Fig. 6, the mesh was refined to a size of 0.1 mm, specifically in the channel-forming region (shown in Fig. 5) to improve accuracy. In the mesh convergence analysis, the reaction force in single-stage forming was considered to evaluate the effect of mesh refinement on the simulation results. While a 0.2 mm mesh also provided good accuracy, a mesh size of 0.1 mm was ultimately selected to more accurately represent local contact conditions.

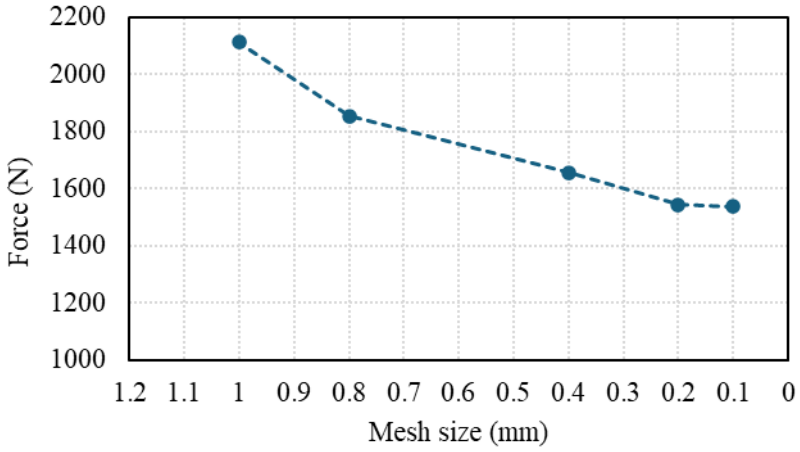

Fig. 6. Mesh sensitivity analysis of the FEA model, showing the influence of the sheet mesh size on the predicted forming force. The reported force corresponds to the reaction force acting on the forming rollers during single-stage micro-roller embossing.

The forming rollers were meshed as deformable bodies with C3D8R elements. A refined mesh size of 0.15 mm was applied in the critical contact locations of the rollers. In the tool corner areas, where the smallest geometric features exist, the mesh was further refined to approximately 0.04 mm to properly capture the geometry. In all other tool regions, the mesh size was set to 1 mm. Symmetry boundary conditions were applied along the centreline, thus allowing only half of the sheet and rollers to be modelled. To define the sheet material properties, an anisotropic Hill48 material model was applied, using the material data from Table 1. The material properties of the rollers were defined based on Fig. 2, using von Mises elasto-plastic isotropic yielding.

The boundary conditions were defined so that the bottom rollers rotated about their axes at 1.5 radians per second, while the top rollers rotated at -1.5 radians (negative indicating the opposite direction to the bottom rollers). In the FEA model, the shafts were modelled as deformable high-strength steel components with high stiffness, rather than as rigid bodies. This approach allows shaft deflection to be captured accurately. The shafts are constrained at the support/bearing locations through the boundary conditions. The interaction algorithm "surface to surface contact" with hard normal contact and Coulomb friction law were defined between the rollers and the sheet surface, and the coefficient of friction was set to 0.2 [21]. The roller embossing process simulation was solved using the ABAQUS/Explicit solver with step time of 3 seconds and a mass scale factor of 5000, resulting in quasi-static conditions with a kinetic energy of less than 10% of the internal energy throughout the forming process. The deformation history of the sheet after the ABAQUS/Explicit steps was imported into ABAQUS/Implicit for a springback analysis. For the springback analysis, all contact conditions were removed to release the formed component in space.

Results and discussion

Single-stage forming. A comparison of the simulation (FEA) and experimental results of the formed part in single-stage forming with equivalent plastic strain (PEEQ) is demonstrated in Fig. 7. This shows close agreement between the simulated and experimental deformed shapes and validates the FEA model predictions.

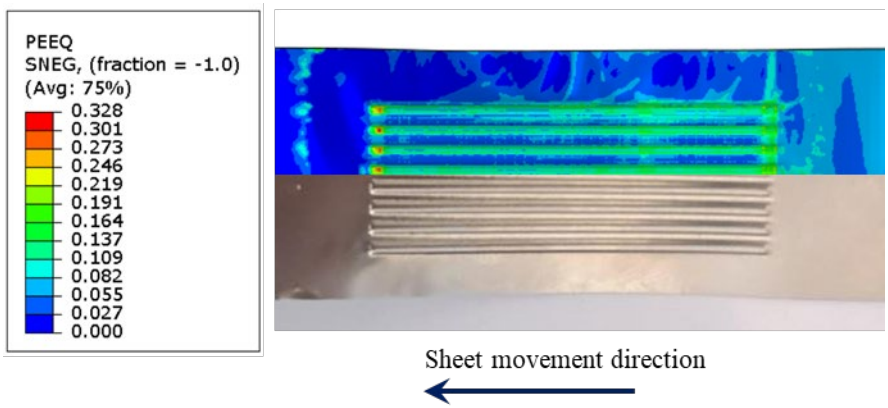

Fig. 7. Comparison of FEA and experimental results of the formed part after the roller embossing process for single-stage forming (target depth = 0.5 mm).

The experimental and the predicted cross-sectional profile shape after forming (and springback) are compared in Fig. 8(b). The comparison is performed using the top surface of the formed part, which is consistently used for all profile evaluations presented in this study. The results indicate that the FEA model can provide a reasonable representation of the experiments. In Fig. 8(b), the first valley shows a small deviation in 2D shape between the experiment and the FEA near the start of the first corrugation (at approximately x=9 mm). In this forming region, the material is not fully constrained by the forming rollers which is different to the symmetry centre area. The thickness distribution of the formed component is shown in Fig. 8(c). For each thickness location, measurements were performed at two corresponding points on two samples. The reported thickness values represent the average of these measurements, and the standard deviation was calculated to quantify experimental variation. The simulation and experimental results are closely aligned and only a small discrepancy exists which may be due to measurement error.

(a)

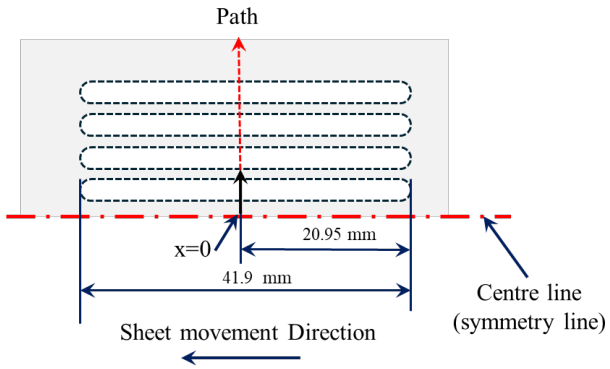

(b)

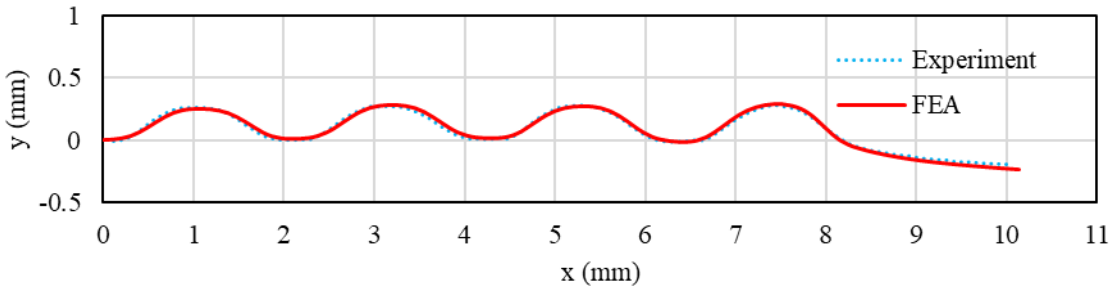

(c)

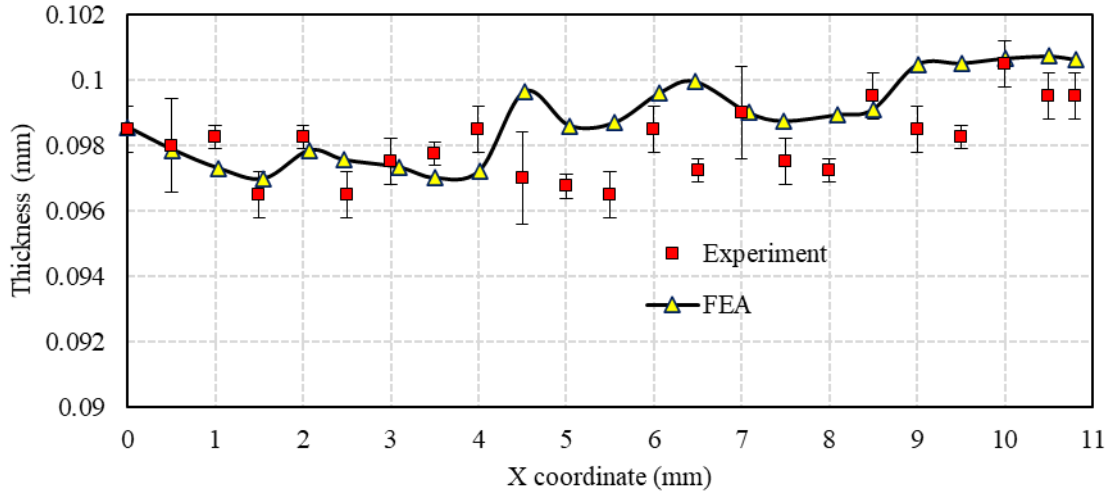

Fig. 8. a) Profile path defined for cross section profile and thinning measurements, b) comparison of the cross-section profile of the formed part between FEA and experiment, c) comparison of the thickness distribution between FEA and experiment.

For the remainder of this paper, for all comparisons, only the profile of the middle channel is considered (Fig. 9(a)), since all channels are relatively consistent as shown in Fig. 8(b). A comparison of the ideal cross-sectional profile and the formed part for single-stage forming (Case A) is shown in Fig. 9(b). The maximum depth of the formed parts was 0.25 mm on average for the eight channels experimentally formed in each part. This result indicates that only 50% of the desired depth was formed and that the channel top had a curved shape instead of the designed (ideal) flat surface.

(a)

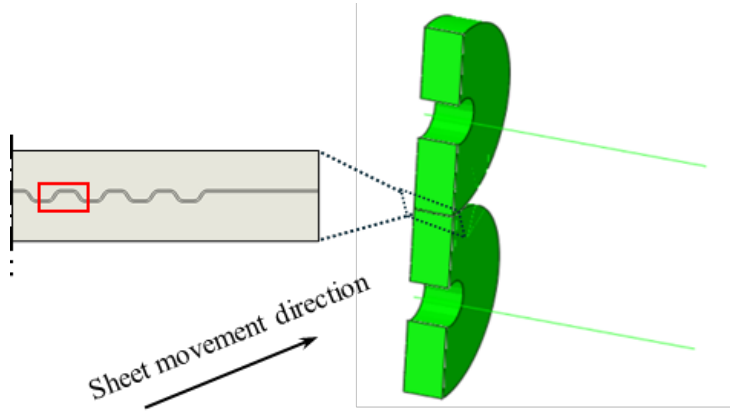

(b)

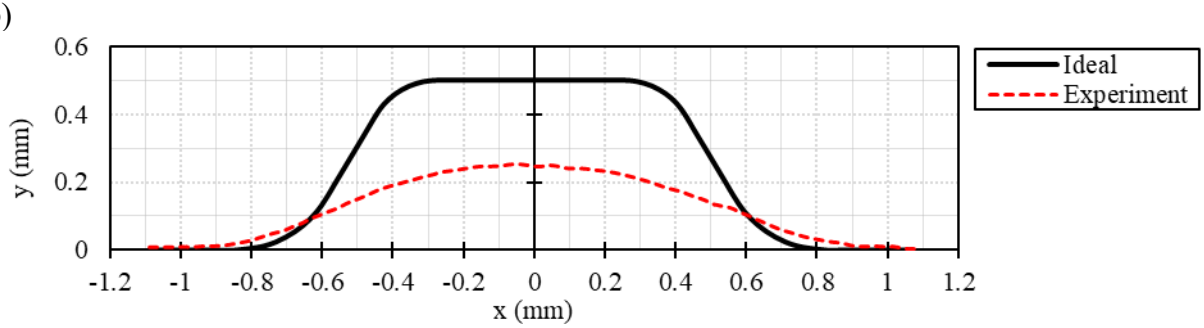

Fig. 9. a) Cross-section of the 3D model, b) FEA cross-section profile of the part compared to the ideal shape for single-stage forming.

Fig. 10 shows a cross-section view of the roller gap (located at the centreline of the rollers), predicted by the FEA model at the location and time where the sheet is positioned between the two rollers. The contour plot shows the equivalent plastic strain (PEEQ) distribution in the rollers. At this location, the rollers should be separated only by the sheet thickness of 0.1 mm. However, the predicted gap is much larger than this (0.292 mm), as shown by the measurements in Fig. 11.

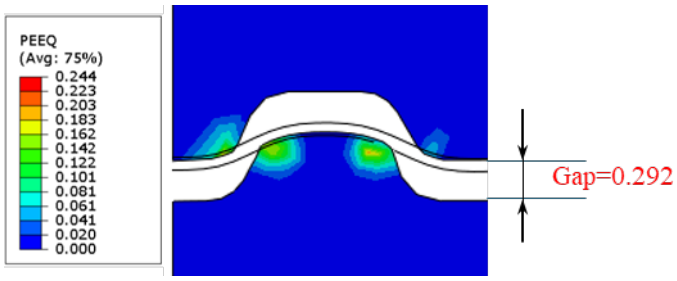

Fig. 10. FEA predicted gap between two rollers at the location where the sheet is formed in the tool gap.

Fig. 10 shows that there is plastic deformation of the rollers near the surface of the roller profiles. However, analysis of the deformation over the entire cross-section of the roller during the forming process revealed that the deflection is not confined solely to this forming region. Instead, the entire roller undergoes deformation (which is mostly elastic deformation). As illustrated in Fig. 11, the roller predominantly experiences deflection in the vertical direction, aligned with the radial direction of the rollers. This deflection prevents full contact between the two roller profiles, contributing to the gap shown in Fig. 10, and limits the maximum achievable forming depth.

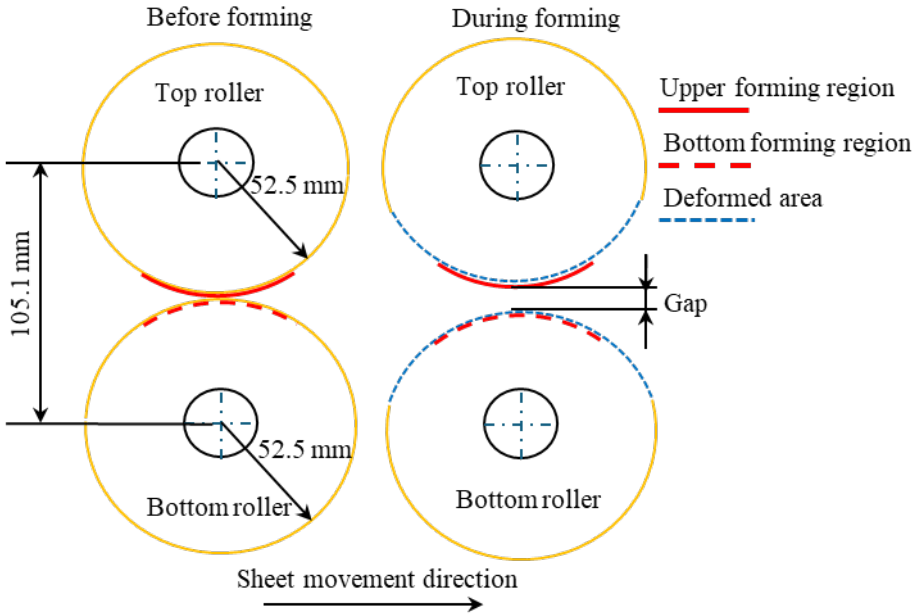

Fig. 11. Schematic illustration of the gap condition between the two embossing rollers during the forming stage.

Another issue is the curved shape of the formed cross-section. One reason for this curvature is that the channel does not reach the designed maximum depth, as shown in Fig. 10 and 11. A second contributing factor is the local deflection of the roller during forming, which results in the deformed shape of the roller profiles deviating from the ideal profile shape. Fig.12 shows the FEA prediction of the two-dimensional profiles for the centre corrugation of the forming roller surfaces at the point where the sheet metal is being formed in the tool gap (for Case A). The black line represents the designed (ideal) roller profile. The results show deflection at the corner radius of the corrugation due to the forming forces, which leads to curvature in the formed channel profile. For this case, the maximum deviation between the ideal and the deformed roller shape is approximately 0.04 mm at the roller corners.

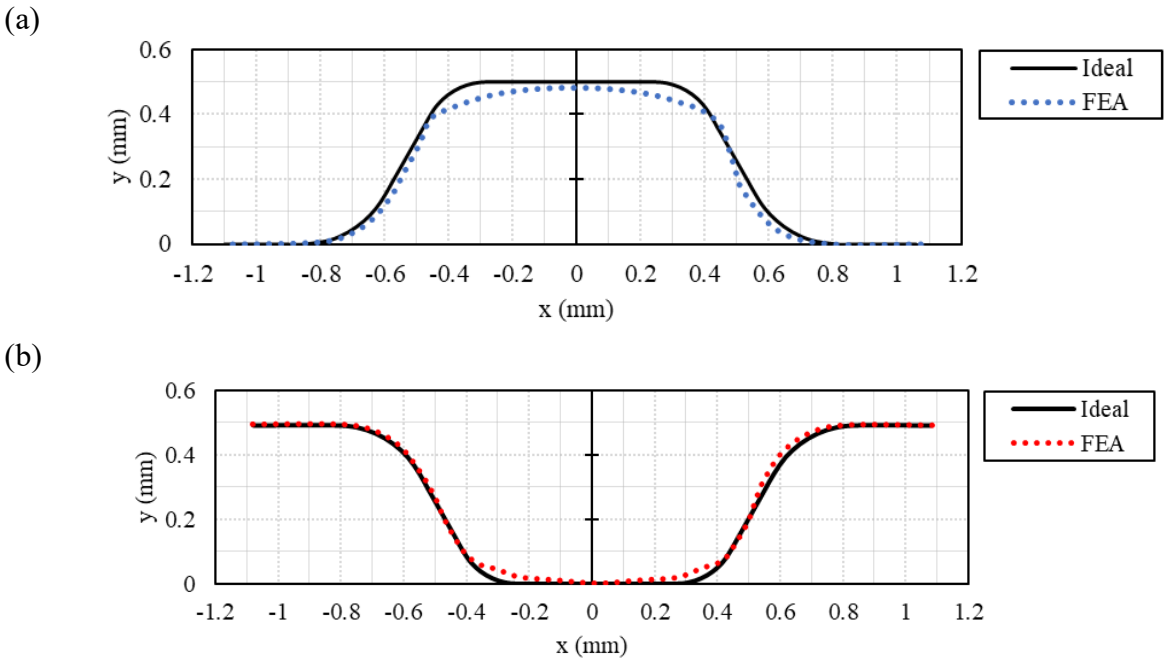

Fig. 12. Cross-section profile of a) top rollers, and b) bottom rollers during the forming stage (for Case A, single-stage forming condition).

Multi-stage forming. A multi-stage forming approach was then applied to try to increase the achievable forming depth, by attempting to reduce the elastic deflection of the entire roller. Instead of a single forming pass, the channels were formed in three stages with target depths of 0.15 mm, 0.30 mm, and 0.50 mm, as shown in Fig. 4(b). In all stages, ABS inserts were used as the forming tools (i.e. Case B in Table 2). This approach led to a reduced roller gap by approximately 17% during forming at the last stage where the target depth is 0.5 mm, as illustrated in Fig. 13(a). Comparison of the effect of the multi-stage forming process is shown in Fig. 13(b). As demonstrated, the forming depth increases from 0.25 mm to 0.30 mm, representing an improvement of approximately 25%.

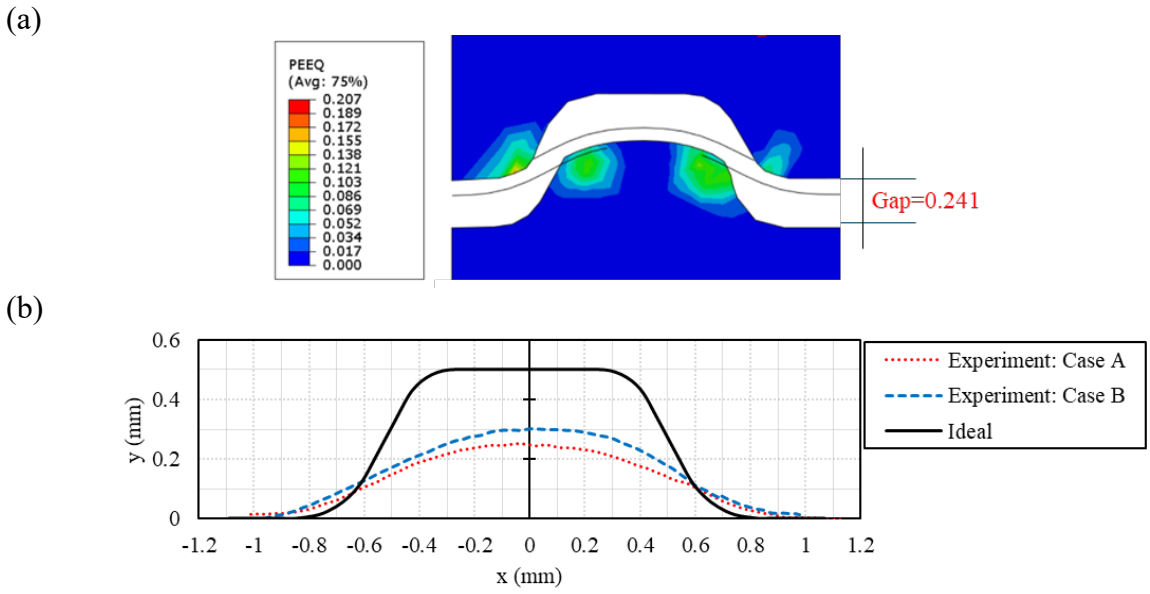

Fig. 13. a) FEA prediction showing a reduction in the tool gap between the top and bottom roller surfaces during the last stage of multi-stage forming (Case B). b) Comparison of the cross-section profile of the formed part with the ideal shape for single and multi-stage forming (experimental results for Cases A and B).

In multi-stage forming, the maximum required forming force is distributed over multiple stages, thereby reducing the stresses that must be transferred by the material. As shown in Fig. 15, this multi-stage forming approach reduces stress concentrations at both the top and bottom rollers. This results

in lower deflection at the corner radii from 0.04 mm (shown in Fig. 12) to 0.03 mm in Fig. 14. Although the reduction in local corner deflection is relatively small, the dominant contribution to the increased forming depth arises from the reduction in global roller deflection, which directly decreases the effective tool gap during multi-stage forming.

The reduction in global roller deflection (Fig. 14 (a) & (b)) leads not only to a smaller effective roller gap (as shown in Fig. 13 (a)), but also to a reduction in local stress concentrations at the channel corners of the rollers (as observed in Fig. 15 (c) & (d)). Consequently, the combined reduction in global tool deflection and local corner stresses enables greater achievable forming depth compared with the single-stage case shown in Fig. 13 (b).

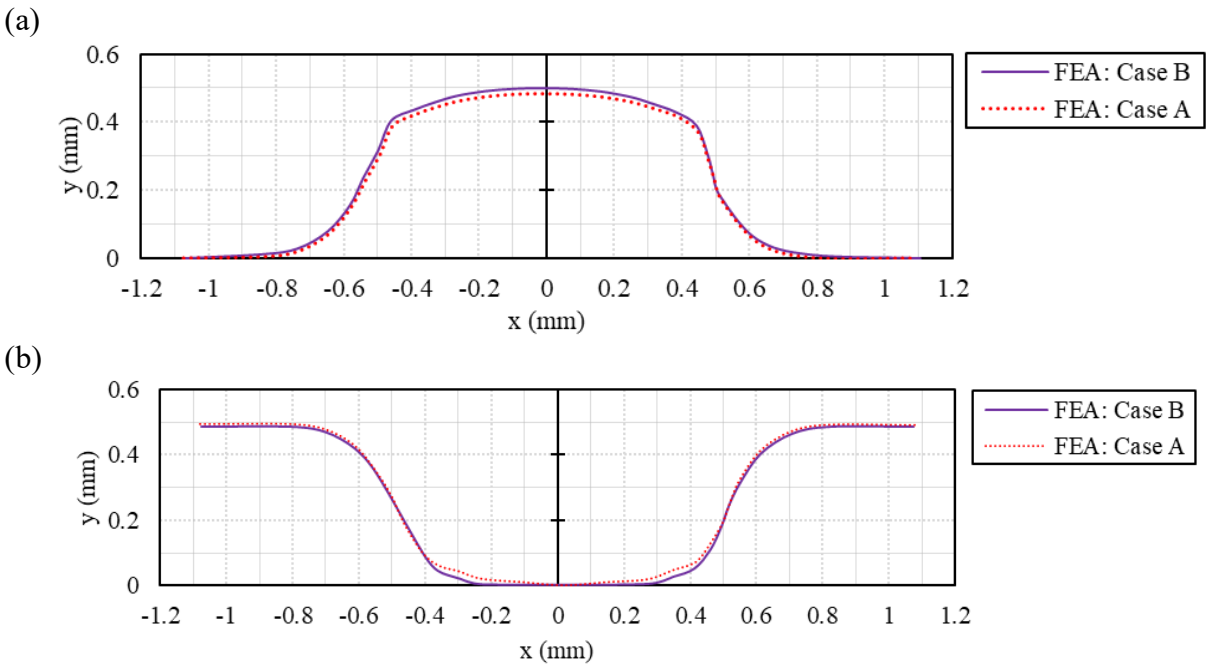

Fig. 14. FEA prediction showing a reduction in corner radius deflection in Case B compared with Case A for a) top roller and b) bottom roller.

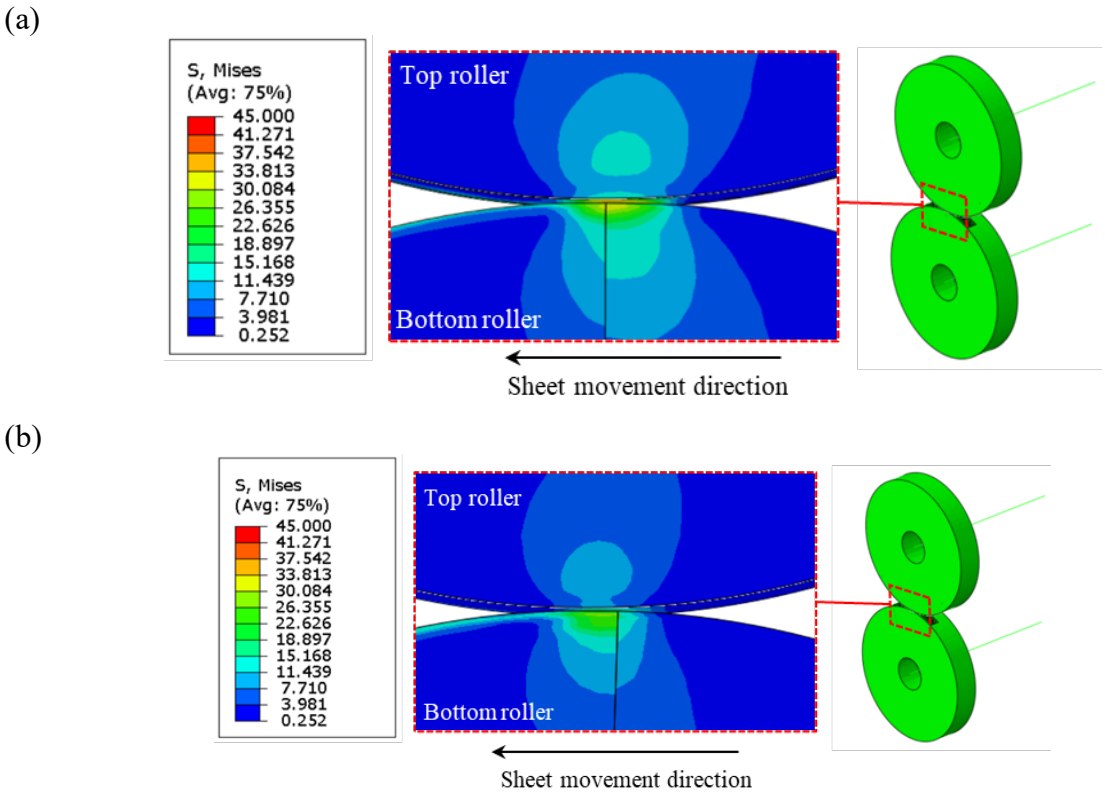

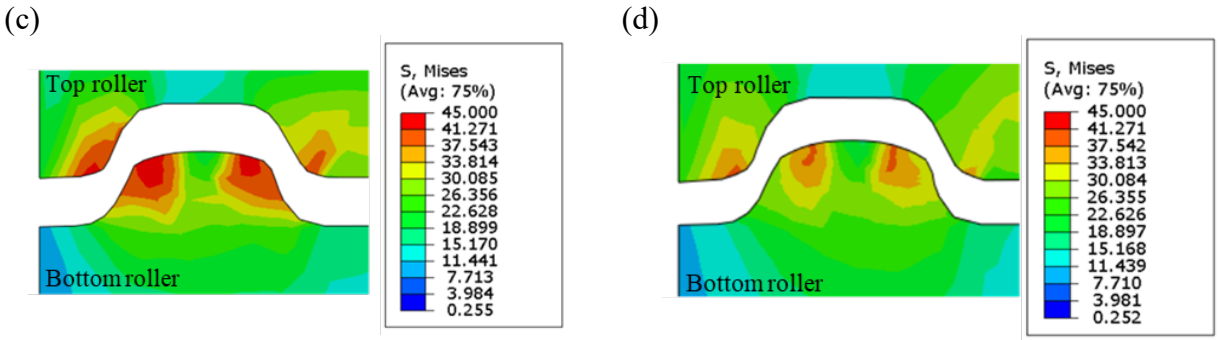

Fig. 15. Von Mises stress distribution [units: MPa] in the forming rollers during a) & c) single-stage forming (Case A), and b) & d) multi-stage forming (Case B), illustrating the reduction in stress concentration at the rollers and the channel corners when deformation is distributed over multiple stages using ABS rollers.

Multi-stage forming with Rigid 10k resin in the final stage. After demonstrating that multi-stage roller embossing increases forming depth, a further study case was conducted in which the multi-stage process was repeated with one key difference: in the final forming stage, a Rigid 10k resin insert was used instead of ABS. The aim was to form channels with tighter corner radii and a flatter bottom surface, due to the higher stiffness of the Rigid 10k material. In this approach, the first two stages acted as pre-forming steps, while the final stage employed a stiffer tool (i.e. Case C in Table 2). The higher stiffness reduced local channel deflection, resulting in a 13% increase in forming depth to approximately 0.34 mm as shown in Fig. 16. However, deflection of the main roller, which was manufactured from ABS, still limited the ability to reach the maximum target depth. In multi-stage forming processes, the creation of pre-shapes increases tool contact during the early forming stages and thereby enhances the maximum transferable stress. This is typically followed by a final forming step in which tight corner radii are produced under lower forming forces. As a result, material is more effectively redistributed during the process, leading to an increased forming depth [22, 23].

The achieved forming depth of 0.34 mm corresponds to approximately 68% of the target profile depth and exceeds the depths reported in previous studies [5] that used steel tools to form the same channel geometry. The 0.34 mm forming depth results in a maximum aspect ratio of 0.314 and also corresponds to much flatter geometry in the channel profiles at the top and bottom surfaces (see Fig. 16).

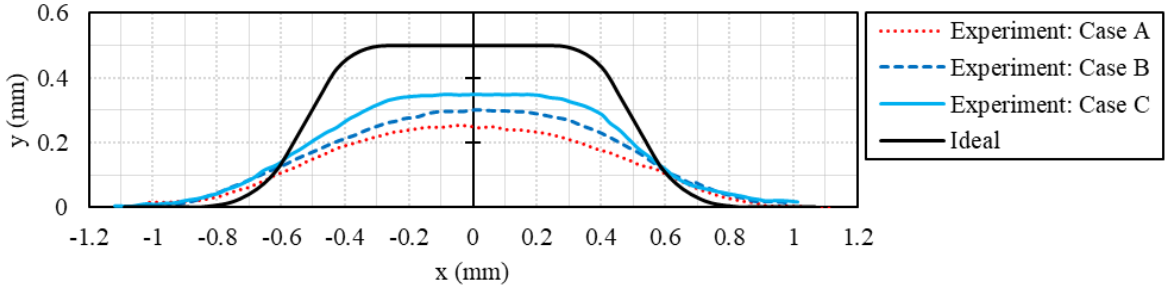

Fig. 16. Comparison of the cross-section profile of the formed part with the ideal shape for single and multi-stage forming (experimental results).

To evaluate repeatability and channel-to-channel consistency, depth measurements were performed for channels 1–4 in the multi-stage forming cases. The FEA results are shown in Fig. 17. The variation across channels is small for both Case B and Case C, indicating uniform deformation across the plate width. The calculated standard deviation across channels was ±0.0205 mm for Case B and ±0.005 mm for Case C, confirming good geometric consistency.

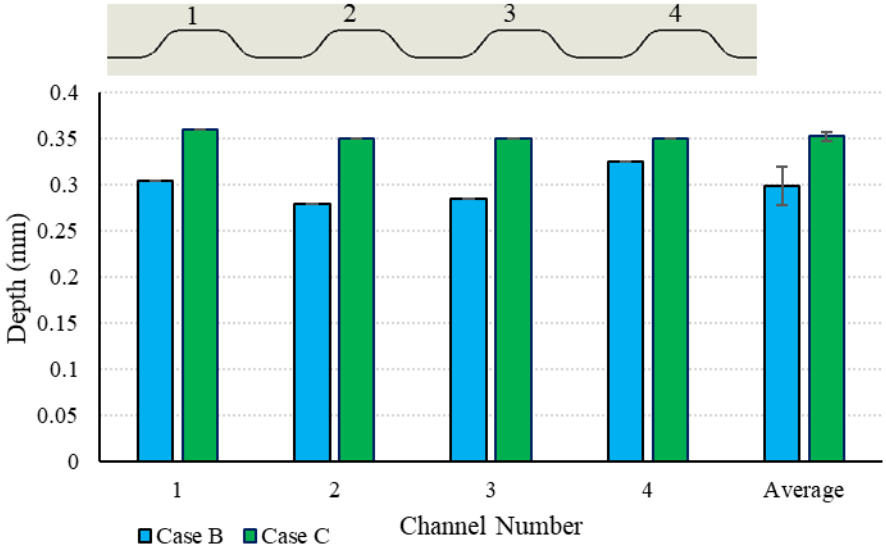

Fig. 17. Channel-to-channel depth distribution for multi-stage forming using ABS inserts (Case B) and hybrid ABS + Rigid 10K resin tooling (Case C). Error bars represent the standard deviation calculated across channels 1–4 for each case.

Table 3 summarises the achieved channel depths and corresponding improvements for the different forming strategies investigated in this study. The results clearly show a progressive increase in forming depth from single-stage forming to multi-stage forming with ABS tooling, and a further improvement when a stiffer resin insert is used in the final stage. This comparison highlights the individual contributions of multi-stage forming and tooling stiffness to improving channel depth. The forming force results in Table 3 further clarify the underlying mechanisms governing channel formation. For ABS tooling, the transition from single-stage to multi-stage forming leads to a reduction in the maximum forming force at the final stage, as the total deformation is distributed over multiple steps and the effective contact stresses are reduced. In contrast, when a stiffer resin insert is employed in the final stage (Case C), the maximum forming force increases despite the improved channel depth. This increase is attributed to the formation of a flatter channel bottom and sharper corner radii, which enhance contact between the sheet and the tool and require higher local forming forces. Nevertheless, the increased stiffness of the resin tool limits tool deflection, allowing the higher forming force to be effectively transferred into material deformation.

Although the use of a stiffer insert improves forming depth, the maximum achievable depth remains limited by global compliance of the roller–shaft assembly. Elastic deflection of the roller body and shafts increases the effective tool gap under load, thereby restricting further depth increase. Future optimisation should therefore focus on stiffening the complete load path, including shafts, roller bodies.

Table 3. Summary of forming depth improvements for different forming strategies

Case	Forming strategy	Tooling configuration	Achieved depth (mm) (average)	Percentage of target depth (0.50 mm)	Relative improvement in forming depth	Maximum forming force at final stage (N)
A	Single-stage forming	ABS inserts	0.25	~50%	Baseline	1921
B	Multi-stage forming (3 stages)	ABS inserts (all 3 stages)	0.30	~60%	25% increase vs. Case A	1610
C	Multi-stage forming (3 stages)	ABS inserts + rigid 10k resin (final stage)	0.35	~68%	13% increase vs. Case B	2665

The results obtained using the Rigid 10K resin insert in the final forming stage suggest that a hybrid tooling strategy may provide further performance improvements. Extending this concept, a hybrid configuration combining polymer-based pre-forming stages with a final metallic finishing pass could further minimise global tool deflection while preserving the flexibility and cost advantages of additively manufactured tools. In such an approach, the polymer tools would be used to generate intermediate channel geometries under reduced load, and a high-stiffness metallic insert in the final stage would ensure accurate corner radii and target depth. This strategy could be particularly attractive for low-volume production or prototyping, where rapid tool iteration is required but final dimensional accuracy remains critical.

Conclusions

A multi-stage micro roller embossing process, relevant to fuel cell bipolar plates, using 3D-printed plastic tools was studied. A FEA model was developed and validated by experimental results and applied to investigate the effect of multi-stage forming on forming depth, and hence aspect ratio. This study demonstrates the feasibility of multi-stage micro-roller embossing of metallic bipolar plate channels using additively manufactured polymer tooling. The results highlight that accurate channel formation requires explicit consideration of tool compliance when applying 3D-printed tools to micro-scale forming processes.

It is possible to use 3D-printed plastic prototype tools for roller embossing microchannel profiles produced from 0.1 mm stainless steel foil. With the initial tool design, the designed channel profile depth was not achieved. This was due to excessive tool deflection, which led to an oversized tool gap between the forming rollers. Using the multi-stage forming, the tooling deflection was reduced. This led to an increase in the achievable channel depth of 25%. In the next step, using tools with higher stiffness in the final stage of forming resulted in a 13% increase in forming depth and improved flatness of the bottom surfaces of the channel profiles.

These findings highlight the importance of accounting for tool compliance in the design of additively manufactured tooling via the simulation of the roller embossing process. To further improve the profile shapes formed, local deflection of the rollers must be accounted for and/or material solutions developed to overcome this deformation**.**

The observed benefits of increased tool stiffness in the final stage indicate that hybrid tooling strategies, combining compliant polymer pre-forming with a high-stiffness metallic finishing pass, represent a promising direction for future work. Such an approach may enable further increases in achievable channel depth while maintaining cost-effective and flexible tooling solutions.

References

[1] P. Zhang, M. Pereira, B. Rolfe, W. Daniel, M. Weiss, Deformation in micro roll forming of bipolar plate, J. Phys.: Conf. Ser. 896 (2017) 012115.

[2] Yang, H., Jiang, T., Xu, Z., & Peng, L., A robust design of the forming process parameters of the metallic bipolar plate for proton exchange membrane fuel cells, Int. J. Hydrogen Energy 47 (2022) 41154–41169

[3] M. Khademi, P. Zhang, M. Pereira, A. Sreenivas, M. Weiss, Finite element model for micro-stamping titanium bipolar plate, Mater. Res. Proc. 28 (2023) 1531–1540.

[4] J.-Y. Koo, Y.-P. Jeon, C.-G. Kang, Effect of stamping load variation on deformation behaviour of stainless steel thin plate with microchannel, Proc. Inst. Mech. Eng. Part B: J. Eng. Manuf. 227 (2013) 1121–1128.

[5] A. Bauer, S. Härtel, B. Awiszus, Manufacturing of metallic bipolar plate channels by rolling, J. Manuf. Mater. Process. 3 (2019) 48.

[6] Reuther, F., Dix, M., Kräusel, V., Psyk, V., & Porstmann, S., Model validation of hollow embossing rolling for bipolar plate forming, Int. J. Mater. Form. 17 (2024) 17.

[7] Z. Xu, Z. Li, R. Zhang, T. Jiang, L. Peng, Fabrication of micro channels for titanium PEMFC bipolar plates by multistage forming process, Int. J. Hydrogen Energy 46 (2021) 11092–11103.

[8] Q. Zhong, R. Hua, C. Wang, L. Cheng, Z. Ma, H. He, F. Chen, Investigation on three-stage stamping of micro-channels with titanium ultra-thin sheet used for PEM fuel cell bipolar plates, Int. J. Adv. Manuf. Technol. 127 (2023) 1377–1389.

[9] T. D. Ngo, A. Kashani, G. Imbalzano, K. T. Nguyen, D. Hui, Additive manufacturing (3D printing): a review of materials, methods, applications and challenges, Compos. Part B Eng. 143 (2018) 172–196.

[10] I. Durgun, Sheet metal forming using FDM rapid prototype tool, Rapid Prototyp. J. 21 (2015) 412–422.

[11] G. Schuh, G. Bergweiler, P. Bickendorf, F. Fiedler, C. Colag, Sheet metal forming using additively manufactured polymer tools, Procedia CIRP 93 (2020) 20–25.

[12] P. Cyron, M. Beck, C. Karadogan, N. Nezic, M. Liewald, Prototype tooling for bipolar plates challenges additive manufacturing, Proc. TMS Annu. Meet. Exhib. (2024) Springer.

[13] P. Zhang, M. P. Pereira, B. F. Rolfe, D. E. Wilkosz, P. Hodgson, M. Weiss, Investigation of material failure in micro-stamping of metallic bipolar plates, J. Manuf. Process. 73(2022)54-66.

[14] Information on https://formlabs.com/materials/.

[15] Information on https://www.stratasys.com/en/materials/materials-catalog/fdm-materials/.

[16] International, A., Annual Book of ASTM Standards, in ASTM D1621-16. 2016.

[17] R. Zou, Y. Xia, S. Liu, P. Hu, W. Hou, Q. Hu, C. Shan, Isotropic and anisotropic elasticity and yielding of 3D printed material, Compos. Part B Eng. 99 (2016) 506–513.

[18] A. Bhattacharjee, T. Loghmani, S. Anwar, Finite element simulation and analysis of drop tests to improve the mechanical design of a handheld QSTM medical device, Proc. ASME Int. Mech. Eng. Congr. Expo. (2022) ASME.

[19] Y. Xu, L. Peng, P. Yi, X. Lai, Analysis of the flow distribution for thin stamped bipolar plates with tapered channel shape, Int. J. Hydrogen Energy 41 (2016) 5084–5095.

[20] A. Essa, B. Abeyrathna, B. Rolfe, M. Weiss, Incremental shape rolling of a variable depth profile, J. Mater. Process. Technol. 316 (2023) 117964.

[21] Z., Mehdiyev, C. Felhő, M. B. Maros, Investigation on production parameters of additively manufactured ABS polymer gears. Cut. Tools Technol. Syst., 97(2022) 91-102.

[22] H. J. Bong, J. Lee, J. H. Kim, F. Barlat, M. G. Lee, Two-stage forming approach for manufacturing ferritic stainless steel bipolar plates in PEM fuel cell: Experiments and numerical simulations, Int. J. Hydrogen Energy 42 (2017) 6965–6977.

[23] M. T. Tran, D. H. Lee, H. W. Lee, D. K. Kim, Formability improvement in multi-stage stamping of ultra-thin metallic bipolar plate for proton exchange membrane fuel cell, Int. J. Hydrogen Energy 47 (2022) 40008–40025.